A multiscale model to understand the interface chemistry, contacts, and dynamics during lithium stripping

Min Feng [a], Xing Liu [b], Stephen J. Harris [c], Brian W. Sheldon [a], Yue Qi [a,*]

[a] *School of Engineering, Brown University, 184 Hope Street, Providence, RI, 02912, United States of America*
[b] *George W. Woodruff School of Mechanical Engineering, Georgia Institute of Technology, 801 Ferst Dr, Atlanta, GA, 30332, United States of America*
[c] *Materials Science Division, Lawrence Berkeley National Lab, 1 Cyclotron Road, Berkeley, CA, 94720, United States of America*

ARTICLE INFO

ABSTRACT

A reversible Li-metal electrode, paired with a solid electrolyte, is critical for attaining higher energy density and safer batteries beyond the current lithium-ion cells. A stable stripping process may be even harder to attain as the stripping process will remove Li-atoms from the surface, and naturally reduce surface contact area, if not self-corrected by other mechanisms, such as diffusion and plastic deformation under an applied external stack pressure. Here, we capture these mechanisms occurring at multiple length- and time- scales, i.e., interface interactions, vacancy hopping, and plastic deformation, by integrating density functional theory (DFT) simulations, kinetic Monte Carlo (KMC), and continuum finite element method (FEM). By assuming the self-affine nature of multiscale contacts, we predict the steady-state contact area as a function of stripping current density, interface wettability, and stack pressure. We further estimate the exponential increase of overpotential due to contact area loss to maintain the same stripping current density. We demonstrate that a lithiophilic interface requires less stack pressure to reach the same steady-state contact area fraction than a lithiophobic interface. A "tolerable steady-state" contact area loss for maintaining stable stripping is estimated at 20 %, corresponding to a 10 % increase in overpotential. To constrain contact loss within the tolerance, the required stack pressure is 0.1, 0.5, and 2 times the yield strength of lithium metal for three distinct interfaces, lithiophilic Li/lithium oxide(Li_2O), Li/lithium lanthanum zirconium oxide(LLZO), and lithiophoblic Li/lithium fluoride(LiF), respectively. The modeling results agree with experiments on the impact of the stack pressure quantitatively, while the discrepancy in stripping rate sensitivity is attributed to the simplifying interface interaction in our simulations. Overall, this multiscale simulation framework demonstrates the importance of electrochemical-mechanical coupling in understanding the dynamics of the Li/SE interface during stripping.

1. Introduction

Solid-state batteries are promising for next-generation batteries due to their usage of non-flammable solid electrolytes (SE) and the Li metal anode with high specific capacity and low electrode potential (Lin et al., 2017; Betz et al., 2019; Zhao et al., 2020; Janek and Zeier, 2023). However, unlike the traditional Li-ion batteries using liquid electrolytes, where the anode is completely immersed in the

electrolyte, the combination of SEs and Li metal anodes results in poor solid-solid contact at the Li/SE interface (Yu and Siegel, 2017; Huang et al., 2020; Tian et al., 2019). Even worse, as Li atoms are removed from the Li-electrode surface during stripping, if the vacancies are not filled by Li flux from the bulk, they will accumulate into voids and reduce the effective contact area for later cycling. After the direct observation of void formation in the Li/Li$_6$PS$_5$Cl (LPSC, Argyrodite) interfaces (Kasemchainan et al., 2019; Liu et al., 2019), Eckhardt et al. further attributed the rate-limiting step at the Li/garnet-type Li$_{6.25}$Al$_{0.25}$La$_3$Zr$_2$O$_{12}$ interface to contact and morphological instability (Eckhardt et al., 2023). The loss of contact not only leads to increasing interfacial overpotential and loss of capacity during stripping but also promotes dendrite growth in the plating cycles due to non-uniform current distribution (Kasemchainan et al., 2019; Liu et al., 2019). This behavior occurs in many other metal-electrode/SE interfaces (Jolly et al., 2020).

Many highly coupled models at the continuum level have been developed to provide a mechanistic understanding of the growth of pre-existing voids or defects (Shishvan et al., 2020; Agier et al., 2022; Barai et al., 2024; Shishvan et al., 2023; Roy et al., 2021; Zhao et al., 2022). Barai et al. (2024) proposed that surface diffusion should be 10^3 times faster than bulk diffusion to prevent/delay void growth. In comparison, Roy et al. (2021) suggested that the diffusion along the Li/LLZO interface was unlikely to enlarge voids and predicted mainly void collapse. Shishvan et al. (2023) also challenged the general belief that the accumulation of vacancies led to void generation if thinning of the electrode was included. The lack of basic parameters used by these continuum models to rationalize the mechanisms may be one of the main reasons for the debate in the literature. Fusing material properties obtained from both experimental data and first principle calculations, such as density function theory (DFT), is extremely valuable in clarifying competing mechanisms.

In this study, we propose that it is more important to quantify the interface contact area for practical battery design, instead of tracking the void evolution. First, the contact area determines the stripping current density and interface impedance, since Li can only be stripped from the regions with intimate contacts. Second, the interface contact is multiscale. Although the initial Li-metal surface may appear flat, it still exhibits multiscale roughness, which will further evolve during cycling. Thus, a pre-existing flaw or void at one scale may not accurately represent the overall surface. Third, this is a highly coupled electrochemical-mechanical dynamics problem, so solving for the contact area is a more tractable problem than tracking the void evolution. Zhang et al. (2020) were the first to predict the contact area evolution at Li/LLZO interfaces under realistic conditions. They sequentially tracked the contact area change caused by plastic deformation, creep, and stripping/plating-induced height variation. Some of their creep properties were interpreted from electrochemical measurements under different stack pressures by Krauskopf et al. (2019).

This problem becomes even more tractable if a "steady-state" interface contact area exists during stripping, as was predicted at the micron-scale by Zhang et al. (2020). Without stack pressure, the increasing interface impedance along with the decreased contact area during stripping form a positive feedback loop that accelerates interface damage and leads to failure. To ensure a "stable" dynamic electrochemical interface, a negative feedback loop is required. Factors, such as Li-metal electrode plastic deformation and Li-atom fast diffusion toward the interface will increase the contact area, thus forming a negative feedback loop to maintain a "stable" contact area. Macroscopically, applying stack pressures is an effective and intuitive method to maintain contact, especially due to plastic and creep deformation of Li metal which are prominent even at room temperature (~ 66 % of the melting temperature of Li-metal). In experiments, commonly used stack pressures are on the order of 10 MPa (Kasemchainan et al., 2019; Wang et al., 2019; Sharafi et al., 2017; Zheng et al., 2021; Liu et al., 2021; Doux et al., 2020). Atomically, interface interactions can be classified into two broad categories based on the resulting wettability against the Li metal: lithiophilic and lithiophobic. For an ideal lithiophilic interface, Li atoms are attracted to the interface to fill the vacancies generated during stripping (Yang and Qi, 2021). Thus, a negative feedback loop can be formed by lithiophilic coating applied on the Li-metal electrode (Liu et al., 2021; He et al., 2022; Ruan et al., 2019; Zhang et al., 2018). In contrast, a lithiophobic interface will enhance a positive feedback loop by trapping vacancies, enhancing void formation, and undermining the contact. (Yang and Qi, 2021; Feng et al., 2022; Yang et al., 2021). Therefore, we hypothesize that such a "negative" feedback loop is necessary to reach a stable interface, which first will be characterized by a "steady-state" contact area that converges to a constant. A "stable" electrochemical interface seems to exist, indicated by stable interface impedance under constant stack pressures at some Li/SE interfaces (Eckhardt et al., 2023; Krauskopf et al., 2019; Wang et al., 2019; Lu et al., 2022). However, the actual contact area has not been quantified experimentally during stripping under different conditions (Krauskopf et al., 2019). As the Li/SE interface is rarely in full contact even before stripping due to surface roughness, it is even more useful to determine a "tolerable steady-state" contact area, both computationally and experimentally.

As mentioned above, the calculation of surface contact area must account for the multi-length-scale nature of surface roughness: from a meter-long Li-metal foil to the atomistic scale, roughness exists at every length scale. Ideally, a statistically accurate description of the surface roughness profile should be used, if available. Such profile information could include the distribution of asperity heights or asperity-asperity distances, on every scale, from at least nano to micro. However, if the statistical properties of the surface roughness profile are different at every scale, as might be supposed, then performing an accurate multiscale analysis of the contact mechanics would be extremely challenging. Surface profiles at the micron scale have been made (Zhang et al., 2020), but no statistical information is available, to our knowledge. On the other hand, making statistically representative nanoscale surface roughness measurements is important but would be especially challenging because of the short length scale of atomic force microscopy (AFM) images.

Fortunately, however, there is considerable evidence that many engineering surfaces are self-affine (or self-similar) fractals (Afferrante et al., 2018; Persson, 2022). This means that certain statistical properties are the same at different length scales. While the initial Li-foil anode surface may appear flat, microstructure images taken for cycled Li-metal surfaces show roughness at many different scales, ranging from nm to mm (Shi et al., 2019). Thus they may have self-affine characteristics. A possible future assumption would be that the statistics of surface profiles at the micron scale can be directly transferred to smaller scales. If this assumption proves valid, then highly accurate multiscale models of contact mechanics, from nano to micron scale, become much simpler. By taking advantage of the fractal nature of many naturally formed surfaces, Persson's multiscale contact mechanics model for elastic materials without

interface adhesion can be used for the cathode/solid electrolyte interface (Afferrante et al., 2018; Persson, 2022). However, no existing multiscale contact mechanics model, spanning from nanometers to micrometers, is currently available to address the plastic deformation and creep of Li-metal under stack pressure. This problem can be simplified since the self-affine property of Li-metal will give rise to statistically "steady-state" surface characteristics (contact area fraction, γ) at each length scale. Thus, instead of integrating stress distribution across different length scales (Persson, 2022), γ can be calculated and connected in the continuum and atomistic levels assuming fractal Li surfaces. At the continuum level (macroscale), γ is the ratio between the effective contact area and the nominal contact area. At the nanoscale/atomic scale, γ is equal to the ratio between the current number of Li atoms on the surface and that of the total Li surface lattice sites.

To construct the multiscale model, simulations need to include different length scales as well as time scales. Based on our previous DFT calculations, the Li vacancy hopping rate is extremely fast in the Li bulk ($1.74 \times 10^{12}\,\text{s}^{-1}$) due to its extremely low hopping barrier (~ 0.05 eV). Combining the Li vacancy formation energy (0.49 eV), the calculated Li bulk diffusion coefficient is $2.8 \times 10^{-11}\,\text{cm}^2/\text{s}$, consistent with experiments, suggesting that it is a carrier (Li vacancy) limited diffusion (Yang and Qi, 2021). However it varies from $10^3\,\text{s}^{-1}$ to $10^{13}\,\text{s}^{-1}$ near the interface due to interface interactions (Yang and Qi, 2021). Compared to the hopping rate, stripping rates ($7\sim8\,\text{s}^{-1}$) for typical current densities (1 mA/cm^2) are much slower. Furthermore, based on the measured creep exponents (n = 6.5), the creep of Li-metal is mainly assisted by dislocation climb in the Li metal, (LePage et al., 2019; Masias et al., 2019) much slower compared to Li hopping (Krauskopf et al., 2019; Wang and Cheng, 2017). Thus different modeling techniques spanning these length scales need to be considered. In the rest of this paper, we propose a coupled modeling method, with density functional theory (DFT), kinetic Monte Carlo (KMC), and finite element method (FEM), to predict the steady-state interface contact area during stripping. With this fully coupled atomic-continuum scale model, we will address the intertwined effects of stack pressure, stripping rate, and interface interaction on the interface contact. Three representative interfaces were considered in this work, the most lithiophilic Li/Li$_2$O interface, the most lithiophobic Li/LiF interface, and the chemically stable Li/LLZO interface. Due to the drastic Li wettability difference between the Li/Li$_2$O and Li/LiF interfaces, their steady-state contact area fractions are expected to show large differences, while the contact at the Li/LLZO interface can be compared with related experiments under varying conditions. In the following manuscript, we will first introduce the computational approach via a "top-down" direction and the results following a "bottom-up" direction.
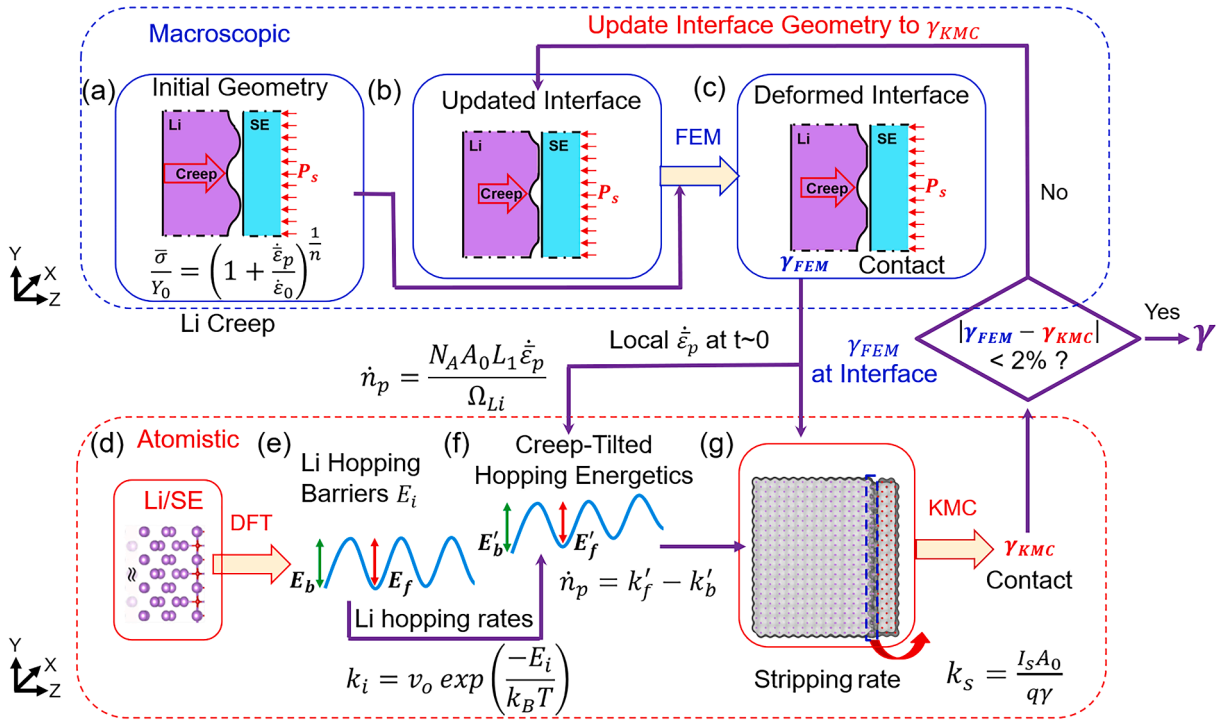

Fig. 1. Schematic of the FEM-DFT-KMC simulation scheme. The top panel illustrates the geometry used in the FEM simulations. (a) The initial geometry to get the representative contact for atomistic KMC simulations. (b) The updated geometry using KMC calculated contact area fraction to start another FEM-KMC iteration. (c) The deformed geometry with the contact area fraction to pass to KMC simulations. The bottom panel describes the DFT-informed-KMC model using FEM output. (d) The optimized atomic interface structure (Li/Li$_2$O here). (e) DFT-calculated vacancy formation energy landscape. (f) Creep-tilted energy landscape. (g) The KMC simulation cell.

2. Computational methods

Fig. 1 demonstrates the coupling of three modeling methods, namely DFT, KMC, and FEM, to predict the steady-state interface contact area during stripping. Table 1 lists the important parameters used in the coupled model. The overarching FEM-DFT-KMC coupling is based on the premise of self-affine contact ($\gamma = \gamma_{FEM} = \gamma_{KMC}$) and the creep-tilted Li hopping energetics. DFT-KMC relies on the FEM prediction of the contact area fraction (γ_{FEM}) and deformed film thickness to update γ_{KMC} while FEM uses the prediction of γ_{KMC} from KMC to make new predictions of γ_{FEM} and further inform KMC. The resulting iterative framework ensures that we can obtain the steady-state contact area fraction (γ) once converged (e.g. $|\gamma_{FEM} - \gamma_{KMC}| < 2\%$).

More specifically, at the macroscale, FEM simulates the Li surface contact evolution under mechanical compression, against a rigid solid electrolyte (e.g. LLZO) subject to creep deformation (pure mechanics) according to experimentally measured constitutive law. Although the engineered surface of the Li anode may appear flat, it has asperities at smaller length scales. Since the actual surface profile and roughness are unknown initially, we assume its self-affine nature, especially during cycling (Persson, 2022). Different from previous models that started from flat surfaces with or without pre-existing voids or surfaces with random roughness (Roy et al., 2021; Zhang et al., 2020; Feng et al., 2022; Yan et al., 2022), the worst-case scenario (point contact) is used as the initial condition. The initial Li surface is assumed to be sinusoidal, while the SE electrolyte surface is flat (Fig. 1a). The Li surface will deform and reach a contact area fraction (Fig. 1c) at the macroscopic scale (detailed in Section 2.1).

The nano-scale Li striping and vacancy hopping and accumulation near the Li/SE interface will be simulated by the DFT-informed-KMC model (Section 2.2). All the atomic interface structures (e.g. a relaxed Li/Li$_2$O interface in Fig. 1d) are optimized using DFT calculations (Section 2.3). The Li vacancy formation energy landscape and the corresponding Li hopping barriers (Fig. 1e) are calculated in the bulk and near the interface. These hopping barriers will lead to Li hopping rates used in KMC models based on the transition state theory (Vineyard, 1957). The initial KMC simulation cells (Fig. 1g) are expanded from the DFT-optimized atomic structures to nanometer scales and used to track the time evolution of vacancy diffusion during stripping. The overall macroscopic creep-induced strain rate is mapped to a creep flux by tilting the Li hopping energy landscape (Fig. 1f) to favor more forward hopping than backward hopping and generates a net creep flux that matches the FEM computed creep rate, $\dot{\bar{\varepsilon}}_p$. There are several other factors that might have secondary effects on the Li hopping energetics and have not been considered in the current model. First, the deformation of the atomic structure used in the KMC model under compressive stress is not considered in the model. Due to the low modulus of Li-metal, the elastic strain energy for 1 % stain is only on the order of 10^{-5} eV, which should have little impact on Li vacancy energy landscapes. We have also evaluated the Li-vacancy formation energy both in the Li-bulk and near the Li/Li$_2$O interface using DFT and found minimal energy change even up to 5 % lattice strain (**Figure S1**). Second, the stress driven vacancy filling is not explicitly modeled. The generation of each Li vacancy during stripping induces a volume decrease, which corresponds to a chemical strain (α). Under hydrostatic pressure p_m, the molar volume difference between a Li-atom (Ω_{Li}) vs a Li-vacancy (Ω_V), can add another driving force ($\Delta\mu_m$) for Li diffusion, $\Delta\mu_m = p_m(\Omega_{Li} - \Omega_V)$. Since our DFT-computed chemical strain is 0.0214 (**Figure S2**), it can be estimated that $\Delta\mu_m = p_m\Omega_{Li}(1 - \alpha^3)$ is less than 10^{-3} eV when p_m is less than 10 MPa. This will not become a significant driving force to push Li to fill the vacancy if the stress is below 10 MPa, compared with the Li-vacancy formation energy of 0.5 eV and hopping barrier of 0.05 eV in the bulk Li.

Iterations between the FEM and KMC models will be carried out to obtain the converged "steady-state" contact area fraction at the two length scales (micrometers vs. nanometers). The macroscale contact area fraction will be used as the initial condition for the KMC model, by randomly removing Li atoms on the surface before the KMC simulation. In the KMC model, the contact area fraction is defined as the fraction of atoms in the first atomic layer, and it evolves with the number of Li atoms stripped and the number of vacancy hopping events. The nanometer scale contact area fraction γ_{KMC} after 10^5 KMC steps will be compared to γ_{FEM}. If the absolute difference between the two values is larger than 2 %, the surface contact area fraction from previous FEM simulations (γ_{FEM}) is modified to be γ_{KMC} (Fig. 1b), and another round of the FEM-KMC loop will be performed. Otherwise, the FEM-KMC loop is terminated, and the "steady-state" contact area fraction is determined. This proposed method did not include the stripping process in the FEM model and thus the

Table 1
Parameters used in the FEM-KMC coupled model.

	Symbol	Definition	Value
Physical constants	k_B	Boltzmann constant	8.617×10^{-5} eV K^{-1}
	T	Temperature	298 K
	N_A	Avogadro's constant	6.022×10^{23} mol^{-1}
	q	Electron charge	1.6×10^{-19} C
Li-metal physical properties	v_0	Vibrational frequency	10^{13} s^{-1}
	A_0	Area for each Li atom on the (100) surface	1.231×10^{-19} m^2
	Ω_{Li}	Li molar volume	13 cm^3 mol^{-1}
Li-metal mechanical properties	Y_0	Li yield strength	0.8 MPa
	$\dot{\varepsilon}_0$	Reference strain rate	0.05 s^{-1}
	n	Power-law creep exponent	6.5
FEM model geometry	L_1	Li anode thickness	100 μm
	L_2	Solid electrolyte thickness	100 μm
	$2W$	Sinusoidal wavelength	8 μm
	h	Sinusoidal amplitude	0.5 μm

contact area will not naturally reduce. Therefore, the initial contact area should be smaller than the "steady-state" for FEM model. A reasonable initial contact area will accelerate KMC model to approach the steady-state.

2.1. FEM simulations

FEM simulations were performed to investigate the macroscale contact between a lithium metal anode with a rough surface and a rigid flat solid electrolyte under moderate stack pressures (Fig. 2). The characteristic wavelength and amplitude of the initial sinusoidal surface roughness for the macroscale contact are $2W$ and h, respectively. The surface roughness is much smaller than the thickness of the Li metal anode. Thus, a two-dimensional (2D) plane-strain model in the y-z plane is formulated utilizing the periodicity and symmetry of the surface roughness (see the green box in Figs. 2**a** and 2**b**) in ABAQUS (Abaqus 2010). We assume the amount of Li stripping is much smaller than that of the Li anode, resulting in a negligible change in the position of the Li/SE interface. Therefore, we applied an *encastré* boundary condition, by constraining all degrees of freedom, to the left surface of the electrode and a constant stack pressure P_s on the right side of the electrolyte and constrained the vertical displacements (along the y-axis) on the symmetric boundaries in both parts. It is worth mentioning that FEM has the potential to simulate a longer stripping process, in which case the fixed boundary should be replaced with a moving one. The contact between the solid electrolyte and electrode was assumed frictionless. The evolution of the contact morphology was monitored, especially the projected/effective contact area and pressure distribution at the interface. Before the converged contact is solved, the surface contact needs to be updated to start the next round of FEM-KMC iteration. The surface morphology was modified by setting the contact region w', which ensures the ratio between w' and chord length W is γ (Fig. 2**b**).

The creep response of lithium metal was described by a phenomenological rate-dependent plasticity model with the Peirce formulation:

$$\frac{\overline{\sigma}}{Y_0} = \left(1 + \frac{\dot{\overline{\varepsilon}}_p}{\dot{\varepsilon}_0}\right)^{\frac{1}{n}}, \tag{1}$$

where $\overline{\sigma}$ is the equivalent tensile stress, Y_0 is the Li yield strength, $\dot{\varepsilon}_0$ is a reference strain rate, and n is the creep exponent. Although the Li yield strength depends on the length scales and temperature, 0.8 MPa is chosen because it is characteristic of Li-metal electrodes with hundreds of μm thickness and in the range for measured values (0.4–1.3 MPa) (LePage et al., 2019; Masias et al., 2019; Tariq et al., 2003; Fincher et al., 2020). To compare with creep laws in other tests assuming different Y_0, the stack pressure was normalized by Y_0, and the stress-strain rate relationship was plotted as a solid line in Fig. 2c in the log-log scale. The power-law creep exponent (n = 6.5, Table 1) and reference strain rate (0.05 s^{-1}, Table 1) were aligned with several experimental measurements of bulk Li (foil and rod) as
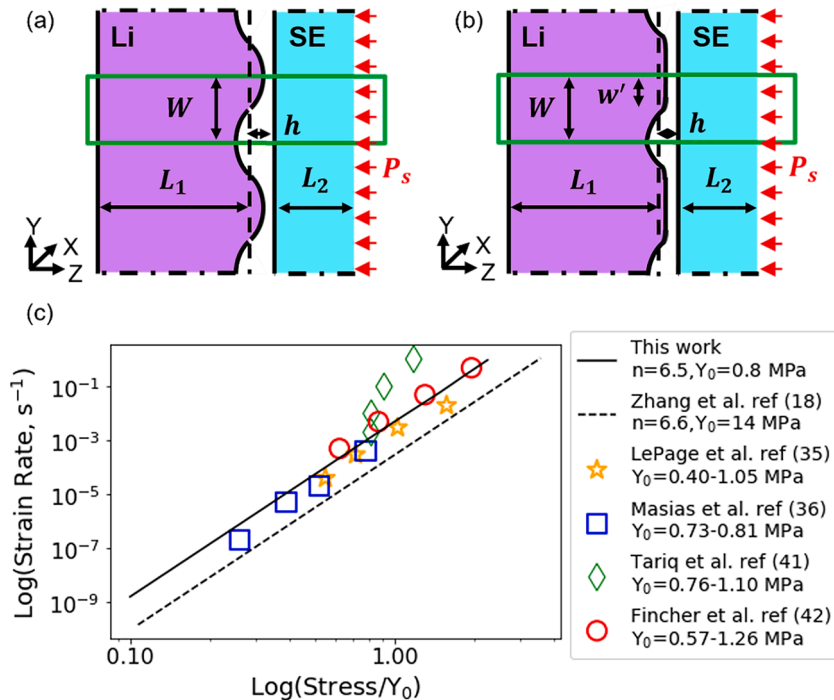

Fig. 2. The initial geometry (point contact) to get the contact area fractions at the nanoscale for KMC simulations (a), the modified surface geometry using the contact area fractions ($\gamma = w'/W$ from KMC simulation (b), the strain rates vs. Normalized stress using Y_0 in log-log scales from experiments and simulations (c).

shown by the markers in Fig. 2c, (LePage et al., 2019; Masias et al., 2019; Tariq et al., 2003; Fincher et al., 2020) and used in simulations by Narayan and Anand (Narayan and Anand, 2018) and others (Shishvan et al., 2020; Shishvan et al., 2023; Shishvan et al., 2021). These pure mechanical tests (LePage et al., 2019; Masias et al., 2019; Tariq et al., 2003; Fincher et al., 2020) (open symbols in Fig. 2c) were performed with strain rates ($\dot{\varepsilon}$) in the range of $10^{-5} \sim 10^{-2}$ s^{-1} below 2 MPa stress. These experimentally used strain rates are relatively ~100 times higher than those fitted to the interface resistance data under an applied stack pressure (the dotted line in Fig. 2c). Zhang et al. used a smaller reference strain rate (2.89×10^{-4} s^{-1}) and a larger Li yield strength (14 MPa) to fit the experimental impedance data that still show changes after hours of stripping. By doing so, their coupled electrochemical and mechanical model has much lower strain rates (dashed line in Fig. 2c), which was explained by the fact that indentation creep is much slower than tensile creep. In our pure mechanics model, taking the mechanical properties directly from mechanical testing is more appropriate (solid line in Fig. 2c). Based on these inputs, the pure mechanical deformation will stop in seconds in the FEM model. This is different from the mechanical response during stripping, which will be captured in the KMC model, where the strain rate is constantly pushing the atoms toward the interface.

2.2. KMC simulations

The KMC simulation cell ($\sim 10^4$ atoms) was expanded from DFT-optimized interface structures. The dimensions were around 55 Å $\times$ 55 Å $\times$ 50 Å, with the z-direction perpendicular to the interface plane. The Li anode comprised a 20-nm bulk region and another 20-nm interface region adjacent to the solid electrolyte. Li atoms on the surfaces were randomly removed to represent the surface contact area fraction obtained from FEM (Fig. 1g). To implement the stripping current density (I_s) in KMC simulations, each Li atom on the surface (or at the Li/SE interface) has a stripping rate of k_s to be removed,

$$k_s = I_s \frac{A_0}{q\gamma}, \tag{2}$$

where q is the charge of a single electron, A_0 is the area of each Li atom on the (100) plane.

In addition to the initial surface vacancies, the stripping events will also generate vacancies at the interface. The corresponding hopping rates (k_i) of Li to fill the vacancies are calculated according to the DFT-NEB calculated hopping barriers in the bulk and/or near the interface without any stack pressures (Vineyard, 1957)

$$k_i = v_o \exp\left(\frac{-E_i}{k_B T}\right), \tag{3}$$

where v_o is the atomic vibrational frequency in solids (10^{13} s^{-1}), k_B is the Boltzmann constant and T is the temperature.

For the mechanical coupling in KMC, the strain rate ($\dot{\bar{\varepsilon}}_p$) is obtained following Eq. (1), but the $\bar{\sigma}$ is simplified by the stack pressure and the contact area fraction, as P_s/γ to capture stress localization near the contact area. The creep strain rates ($\dot{\bar{\varepsilon}}_p$) is assumed to create a creep flux ($\dot{n}_p$) to alter the Li hopping rates following

$$\dot{n}_p = \frac{N_A A_0 L_1 \dot{\bar{\varepsilon}}_p}{\Omega_{Li}} \tag{4}$$

where N_A is the Avogadro constant, L_1 is the deformed thickness of the Li anode (from the back to the contact point) updated by the
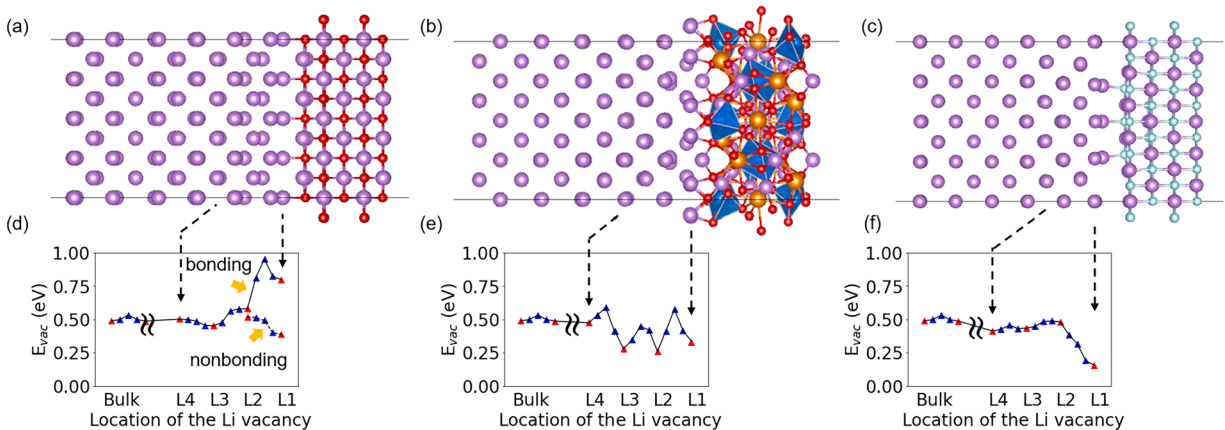

Fig. 3. Optimized asymmetric interface structures for (a) Li/Li$_2$O, (b) Li/LLZO, and (c) Li/LiF, corresponding to wetting angles of 0°, 60.2°. and 108.7°, respectively. The calculated vacancy formation energy landscape is shown below each structure. For Li/Li$_2$O (d), curves for both bonding and nonbonding Li atoms are plotted. For Li/LLZO (e) and Li/LiF (f), only bonding curves are shown due to the similar shapes of the energy landscape. Cutoff distance for bonding atoms: 2.2 Å. Purple: Li, Red: O, Blue: Zr, Orange: La, Cyan: F.

FEM simulations. As the creep flux assists Li diffusion toward the interface, it is equivalent to a lowered forward hopping barrier (E'_f) and an increased backward hopping barrier (E'_b), and the difference between the modified forward and backward hopping rates gives rise to the creep flux, as

$$\dot{n}_p = v_0 \exp\left(-\frac{E'_f}{k_B T}\right) - v_0 \exp\left(-\frac{E'_b}{k_B T}\right). \tag{5}$$

Let E_p denote the creep-induced change in the difference between forward and backward hopping barriers. Assume creep tilts the forward and backward hopping barriers (E_f, E_b) symmetrically, the modified forward (E'_f) and backward (E'_b) hopping barriers are given by

$$E'_f = E_f - 0.5E_p, \tag{6a}$$

$$E'_b = E_b + 0.5E_p. \tag{6b}$$

$$E_p = 2k_B T \ln\left[\frac{\dot{n}_p + \left(\dot{n}_p{}^2 + 4k_f k_b\right)^{\frac{1}{2}}}{2k_f}\right] \quad (\dot{n}_p > 0, \; P_s > 0). \tag{6c}$$

E_f and E_b can be obtained from DFT calculations (shown in Fig. 3). This treatment was developed in our previous work and managed to capture the creep effects on the vacancy evolution near the Li/Li$_2$O and Li/LiF interfaces (Feng et al., 2022). When using modified hopping rates to evolve the interface structure, both interface interactions and creep effects are incorporated into KMC simulations.

The KMC simulation code is designed according to the Bortz-Kalos-Lebowitz (BKL) algorithm in Fortran 90 (Bortz et al., 1975). The details were mentioned in previous work (Yang and Qi, 2021; Feng et al., 2022) and these references (Andersen et al., 2019; Gavilán-Arriazu et al., 2021). The contact area fraction from KMC (γ_{KMC}) will be compared with γ_{FEM} based on the criteria of 2 % absolute difference to decide whether the equilibrium contact across different length scales is reached.

2.3. DFT: Interface calculations

All plane-wave DFT calculations were performed with the Vienna Ab initio Simulation Package (VASP). Perdew−Burke−Ernzerhof (PBE) functionals with the generalized gradient approximation (GGA) were used for the exchange correlations (Perdew et al., 1996) The interactions between the core and the valence electrons were described by the projector augmented wave (PAW) method (Joubert, 1999; Mortensen et al., 2005). A cutoff energy of 600 eV and K-point density of 0.03 Å^{-1} ($3 \times 3 \times 3$ K-point grids) were tested to be sufficient for all bulk structures to reach 1 meV/atom convergence. The energy convergence of 10^{-5} eV and the force convergence of 0.03 eV/Å were used for electronic structure and atomic structure minimization. The Gamma point and Gaussian smearing were used in all interface calculations. The computational approach followed our previous work on Li/Li$_2$O and Li/LiF interfaces. The DFT results (Fig. 3) on these two interfaces were replotted for comparison with the Li/LLZO interfaces computed in this work (Yang and Qi, 2021; Feng et al., 2022).

The Li/LLZO interface was constructed using the Li (001) surface and the LLZO Zr-rich-(001) surface (more under-coordinated O for stronger interface bonding). The construction of the LLZO surfaces was described in the **SI** and shown in **Figure S3**. All the surface energy is listed in **Table S1**. The in-plane dimensions (the *x-y* plane) of the interface slab are 13.134 Å × 13.134 Å, which ensures the strain for the Li is smaller than 5 % (-4.64 %) in both directions. A symmetric interface without vacuum layers was constructed to calculate the work of adhesion and the interfacial wettability, where 13 layers of Li were used. The work of adhesion (*W*) is defined as $W_{ad} = \frac{1}{2A_i}[E_{slab(LLZO)} + E_{slab(Li)} - E_{tot}]$, where A_i is the in-plane area of the interface, $E_{slab(LLZO)}$ is the energy of the LLZO surface slab, $E_{slab(Li)}$ is the energy of the Li slab and E_{tot} is the total energy of the interface. The wetting angle θ is related to the work of adhesion according to $\cos\theta = \frac{W_{ad}}{\gamma_{Li}} - 1$, where γ_{Li} is the Li (001) surface energy (0.42 J/m^2). The calculated work of adhesion for the Li/LLZO interface is 0.63 J/m^2 (wetting angle 60.2°), comparable to the reported values (Sharafi et al., 2017).

To save the computational cost, asymmetric models (Fig. 3) with vacuum layers were employed to calculate the vacancy formation energy (E_{vac}) and hopping barriers (E_i), where 11 layers of Li were used and the outermost three layers of Li were fixed to represent the bulk region. The vacancy formation energy (E_{vac}) is calculated using $E_{vac} = E_v + \mu_{Li} - E_{tot}$, where E_v is the interface structure with one Li vacancy, μ_{Li} is the Li chemical potential (-1.904 eV). The hopping barriers for Li vacancies along the (111) direction in the interface were calculated using the Nudged Elastic Band (NEB) method (Henkelman and Jónsson, 2000) with three transitional configurations between the initial and final structures.

3. Results and discussions

3.1. Interface structures, interaction and vacancy formation energy landscape from DFT

The asymmetric interface structures with 11 Li layers for the three interfaces are shown in Fig. 3 (a-c). The corresponding vacancy formation energy landscapes are plotted in Fig. 3 (d-f). In all systems, due to interface interactions, the first few Li layers near the interface do not form the perfect body-centered cubic (bcc) structure as the bulk. Using 2.2 Å as a cutoff to describe the distance between Li atoms on the first layer (L1) and the anions in the solid electrolyte, the Li atoms can be classified as bonding and

nonbonding, which are more obvious in the Li/Li$_2$O and Li/LiF interfaces. The hopping barriers of bonding and nonbonding atoms are calculated for each. For the lithiophilic Li/Li$_2$O interface (Fig. 3a), the bonding atoms show strong interactions with the electrolyte so that E_{vac} on L1 is around 0.3 eV higher than the bulk value (0.50 eV), suggesting when vacancies are generated during stripping, they can be filled by the Li hopping from L2, as the forward hopping barrier is much smaller than the backward value (Fig. 3d). In comparison, nonbonding atoms show E_{vac} smaller than the bulk value, which means vacancies prefer to form and stay at the nonbonding sites. For the lithiophobic Li/LiF interface (Fig. 3c), both bonding and nonbonding atoms (only bonding atoms are shown due to similar curves) are repelled from the interface as E_{vac} at the interface is at least 0.2 eV lower than that in the bulk (Fig. 3f). As a result, when vacancies are generated on the surface, they will stay at the interface, leading to poor contact. In terms of the Li/LLZO interface, Li atoms on the surface are rearranged in a way resembling reported relaxed Li/LLZO structures (Burov et al., 2024), but the bonding and nonbonding atoms do not show significant differences in E_{vac} or hopping barriers. It is apparent that LLZO causes more influence on the vacancy formation energy landscape, as E_{vac} in the first three layers is lower than the bulk value. These E_{vac} fall in the range from 0.25 to 0.35 eV, comparable to reported values in similar Li/LLZO interfaces (Burov et al., 2024). The lower E_{vac} on L2 and L3, and even L1, suggests Li atoms will jump in either direction (left or right) with almost equal probability like the scenario in the Li bulk (but slower). Therefore, vacancies are not expected to show a clear tendency of being filled or trapped on the surface, but rather form a distribution among the first few layers, revealing its Li wettability between Li/Li$_2$O and Li/LiF.

3.2. Implementation of the constant current density and creep effects in KMC simulations

The stripping process is first implemented in the KMC model along with all the Li hopping events with no stack pressure. The orange circles in Fig. 4 (a-c) are the number of stripped Li atoms, which increases linearly with time, consistent with the stripping current density (I_s) being implemented. The high current density here accelerates the stripping events so that sufficient Li atoms are removed and compared in one KMC test for all interfaces. Other stripping current density results can be found in **Figure S4 in SI**. The stripping current remains constant despite different contact morphologies emerging during the KMC simulations. The inserts in the left corner of Fig. 4 (a-c) show the Li atoms in the first layer at the end of the KMC simulations and the black area represents the contact region, as γ, and the evolution of vacancy fractions (1-γ) is also shown in Fig. 4 (a-c) (as the black circles). The interface interactions lead to different contact area fractions in the absence of stack pressure. In the Li/Li$_2$O interface (Fig. 4a), the contact area fraction decreases when stripping starts, but remains stable at around 75 % due to rapid forward hopping. In contrast, at the Li/LiF interface (Fig. 4c), because of the much larger forward barriers, Li vacancies cannot be filled instantly, and the contact continues to decrease until it becomes zero, where there are no Li atoms and stripping terminates. As revealed in the wettability ranking, the Li/LLZO interface can maintain a constant contact area fraction between the other two interfaces.

To demonstrate that a "steady-state" surface contact area is possible, we started from interfaces with full contact and point contact, respectively. Fig. 4 (a-c) started from full contact. The interface interaction can be seen even more clearly when stripping starting with
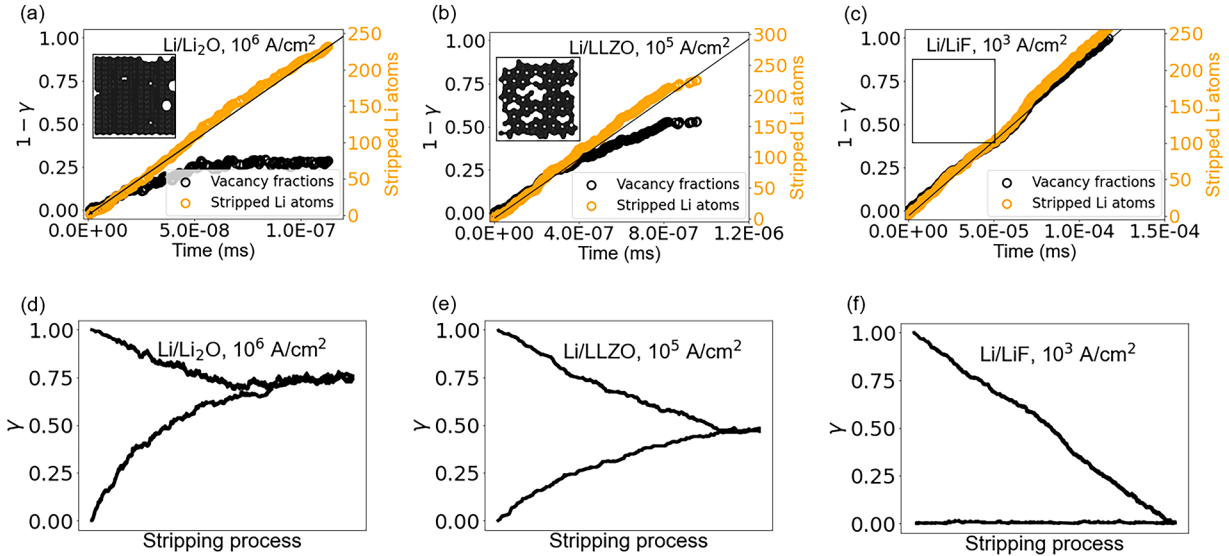

Fig. 4. Dimensionless contact area fraction (γ) and loss of contract area fraction (1-γ). Upper panel: KMC simulations of loss of contact during stripping at constant current densities without creep for (a) Li/Li$_2$O, (b) Li/LLZO, and (c) Li/LiF. The atomic surface contacts after 10^5 KMC steps are inserted in the upper left corner and the black portions are the contact area. The solid line represents the theoretical stripped number of Li atoms over time. Lower panel: The evolution of the contact area fraction (γ) during stripping (with the same time scales as the upper panel) starting from two initial values, 0 % (lower curves) and 100 % (higher curves), respectively. To reach steady state, fast stripping current densities associated with different interfaces were used: 10^6 A/cm^2 (a and d), 10^5 A/cm^2 (b and e), 10^3 A/cm^2 (c and f). Other stripping current density results can be found in Figure S4 in SI.

the point contact (lower black lines) is compared to the case with 100 % initial contact (higher black lines) in Fig. 4 (**d-f**). The γ at the Li/Li$_2$O interface will increase to 75 %, the same value when starting from 100 % contact. In the other two interfaces, γ also converges to 48 % (Li/LLZO, Fig. 4**e**) and point contact (Li/LiF, Fig. 4**f**), respectively, regardless of the original contact. This confirms our initial hypothesis that there is a steady-state contact area fraction that is determined by the interface wetting properties. Thus, a more lithiophilic interface leads to a higher steady-state contact area fraction. It is important to note that Fig. 4 shows a pressure-free example. The steady-state contact area will be altered when a stack pressure is applied. In such circumstances, we need to adopt the coupled model (Fig. 1) to predict the steady state. We demonstrate the significance of the FEM-DFT-KMC coupling by comparing the result of the coupled model with that of the pure KMC model for the Li/LiF interface at a stack pressure of $0.1Y_0$ and a current density of 1 mA/cm^2 (**Figure S5**). The coupled model predicts a steady-state contact area fraction of ~30 % while the pure KMC model predicts 89 %. A reasonable estimation based on the reported value for the more lithiophilic Li/LLZO interface is <30 %, (Eckhardt et al., 2023) in favor of the coupled model. The failure of the pure KMC model is attributed to the fact that it has not properly accounted for the initial contact area and the creep-induced tilt in the Li hopping energetics. Therefore, the coupling between FEM and DFT-KMC is crucial to the reliable prediction of the steady-state contact area fraction.

With the proper implementation of the stripping rate under the corresponding current density (Eq. (2)), the creep effects are incorporated as the mechanical bias (E_p) into the hopping barriers to perform KMC simulations of the contact evolution (Eqs. (5) and (6)). Fig. 5 compares the contact area fraction evolution with and without creep effects using a starting contact area fraction of 62 % under 1 mA/cm^2 within one KMC test. The applied stack pressure is $2Y_0$. The black curves in these figures correspond to contact without creep effects. The contact here is not at the steady state because it cannot reach the equilibrium within 1 KMC test under a much smaller current density compared to those in Fig. 4. Instead, it further illustrates how these surfaces evolve under the impacts of interface interactions. The contact area fraction of the lithiophilic Li/Li$_2$O shows an increase of around 25 %, while the less lithiophilic Li/LLZO gained 10 % in contact area fraction, while that of the lithiophobic Li/LiF remains almost unchanged. When creep effects are considered ($P_s = 2Y_0$), the contact in Li/Li$_2$O (the red curve in Fig. 5**a**) increases to nearly 100 % and the contact in Li/LLZO (the green curve in Fig. 5**b**) and Li/LiF (the blue curve in Fig. 5**c**) increases to 85 % and 75 %, respectively. Therefore, the creep effects will provide additional Li flux to the interface in the microscale in a short period and should be included in the KMC simulations. In the following FEM-KMC iterations, different initial contact configurations are used to determine the stable contact regions under stack pressures.

3.3. The "steady-state" contact area fraction at both macroscale and microscale

Fig. 6 shows the iterations of FEM and KMC models to reach the "steady-state" contact area fraction at the two length scales. Starting from the point contact (the worst-case scenario), the FEM simulations tracked the initial contact area fraction increase under different stack pressures in the first frame (more pressures are shown in **Figure S6a** in **SI**). As there are debates about the yield stress of Li-metal, the stack pressure has been normalized with the yield stress. Even the $0.1 Y_0$ curve causes the increase in the contact (from almost 0 % to 4 %) and the $1.0 Y_0$ curve shows an increase to 38 %, which suggests any amount of stack pressure is generally beneficial in maintaining the interface contact. The contact area fraction at the end of the FEM is then passed into KMC simulations to construct the starting surface configurations subjected to stripping currents.

The corresponding KMC results are shown in the second frame in Fig. 6. Since the initial contact area is low, Li hopping increases the contact for all three surfaces, even when the stack pressure is as low as $0.1 Y_0$. The more lithiophilic the interface is, the higher the contact area, which is the same case for the $1.0 Y_0$ curve. When comparing the contact after KMC simulations, the Li/Li$_2$O can reach almost full contact even under the stack pressure as low as $0.1 Y_0$. Here 10^5 steps of KMC models are performed, then the contact area fraction is passed to the FEM model again.

The contact evolutions under different stack pressures change minimally as shown in frame 3 in Fig. 6 (more details in Figure S6b and S6c in SI). Within the stack pressure range ($0.1Y_0$ -$2.0Y_0$), the creep effects do not cause significant changes to the contact area fraction after the 1st iteration, which suggests the creep under compression decays over time as observed in experiments (Masias et al., 2019) and the contact will converge when it eventually reaches the steady state (Fig. 6, the last frame).

Our main goal is to determine the steady-state contact area fraction, so the time in the FEM and KMC iterations shown in Fig. 6
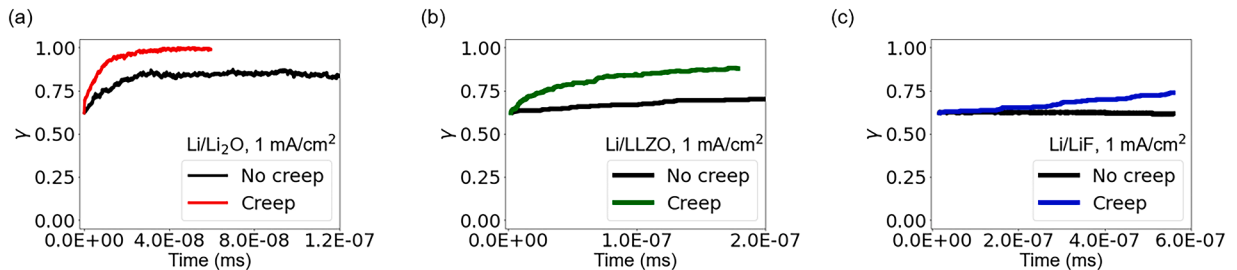

Fig. 5. The comparison between KMC simulations of contact evolution with and without creep effects for (a) Li/Li$_2$O, (b) Li/LLZO, and (c) Li/LiF under 1 mA/cm^2. The black curves are results without creep, while the red curve in (a), green curve in (b), and blue curve in (c) are results under a stack pressure of 2 Y_0.
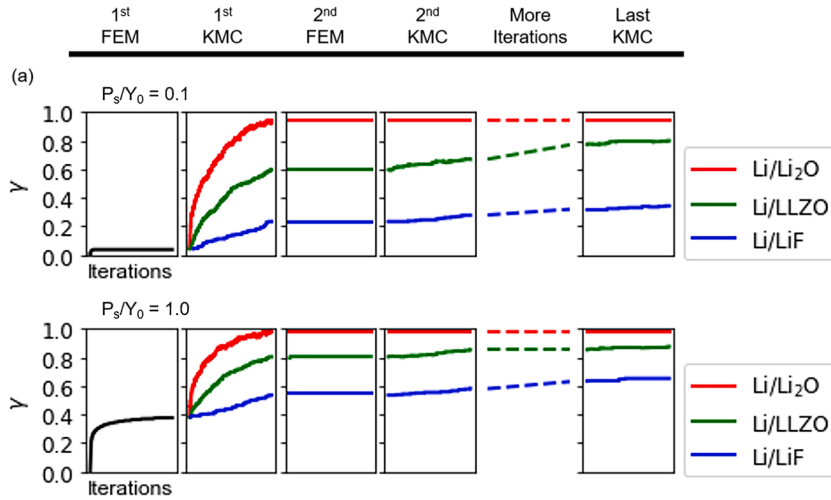
Fig. 6. The iterations of FEM and KMC models on contact area evolution at two contact pressures (a) $0.1 Y_0$, (b) $1.0 Y_0$ and three different interfaces under 1 mA/cm^2. Red: Li/Li$_2$O, green: Li/LLZO, and blue: Li/LiF. The time scale for FEM is ~1s. The time scale for KMC models is 10^5 KMC step. The focus should be the converged steady state contact area fraction (γ), instead of the evolution process.

should not be interpreted as stripping time, which is different from Wang et al. (2019) and Zhang et al. (2020). It is worth noting that although the mapping between the stack pressure and the contact is clear in our model and other papers, the way to interpret the time scales of creep effects can be different. In Wang's paper, (Wang et al., 2019) they observed a decreasing contact after 32 hours of stripping, thus they scaled material-specific creep parameter (7×10^{-37} Pa$^{-6.5}$s^{-1}) by 10^{-4} for all the measured creep data in their model. A similar scaling strategy was also adopted in Zhang et al. (2020) work. This seems to suggest the creep would have happened in hours. However, per the experimentally tested Li-metal mechanical properties, the time scales of creep response occur much faster. Wang et al. ascribed to the decrease of the strain rate due to frictional and adhesive forces at the interface. While these are reasonable, if interface damage (e.g. metallic Li becomes oxide) occurs over time, the creep rate will decrease accordingly. This possibility will be further discussed in the next Section.
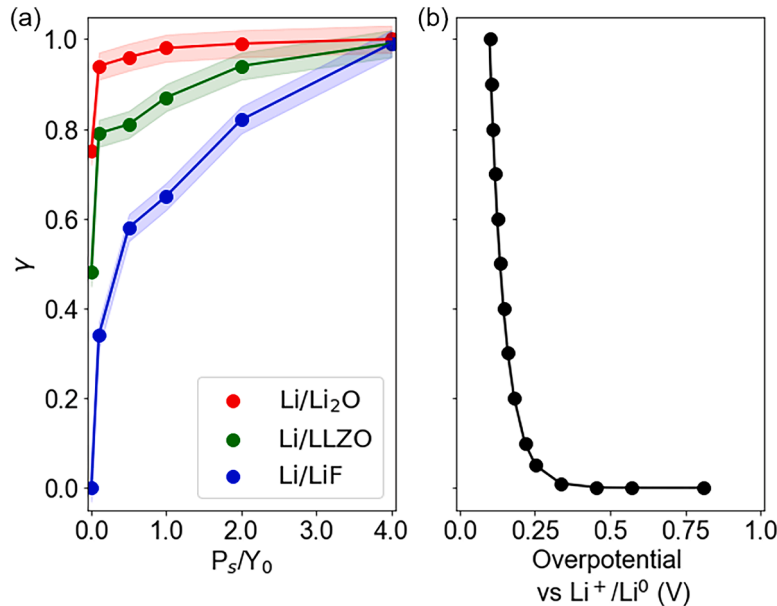

Fig. 7. The steady-state contact area fraction for three interfaces under different stack pressures under stripping current densities between 1 and 10^3 mA/cm^2. (a) and the effective overpotential required to maintain the same current density with initial 100 % contact and an overpotential of 0.1 V. (b) Red: Li/Li$_2$O, green: Li/LLZO, and blue: Li/LiF.

3.4. The steady-state contact and corresponding overpotentials

Fig. 7 showing both the contact area change with stack pressure and the resulted overpotential increase can help to analyze the intertwined electrochemical and mechanical effects. Fig. 7a shows the steady-state contact for three interfaces under different stack pressures. The error bars ($\pm$ 0.02) in Fig. 7a are determined based on results under stripping current densities between 1 and 10^3 mA/cm^2. When there is no stack pressure, the contact is impacted by the interface interactions and follows the trend Li$_2$O > LLZO > LiF. The extremely fast Li diffusion near the interface discussed by Barai et al. (2024) is consistent with the fast Li diffusion at the extremely lithophilic Li/Li$_2$O interface. When the stack pressure is applied, it contributes to the contact even when it is only 0.1 Y_0. The influence of the stack pressure and creep effects is more prominent for the lithiophobic Li/LiF interface, the contact of which is increased by over 30 % under a small stack pressure, $P_s = 0.1Y_0$. It is ascribed to the modified hopping barriers, where the forward barrier is always smaller than the backward value so that more Li atoms are pushed towards the surface to increase the contact area.

Many battery tests have been performed with a constant current density I_s. Similar to what has been implemented in the KMC model, the effective striping rate needs to be scaled with the true contact area, since Li can only be stripped from areas in contact. Similar to Eq. (2), the macroscopic effective stripping current density (I_{eff}) must increase with decreasing contact area fraction, $I_{eff} = I_s$ /γ. Assuming the stripping reaction follows Bulter-Volmer kinetics and I_s is the stripping current density at 0.1 V overpotential with 100 % contact, to maintain the same I_s, a larger overpotential, η_{eff}, must be applied to achieve a higher I_{eff}.

$$\frac{1}{\gamma}\left[\exp\left(\frac{\alpha F 0.1}{k_B N_A T}\right) - \exp\left(-\frac{(1-\alpha)F 0.1}{k_B N_A T}\right)\right] = \left[\exp\left(\frac{\alpha F \eta_{eff}}{k_B N_A T}\right) - \exp\left(-\frac{(1-\alpha)F \eta_{eff}}{k_B N_A T}\right)\right], \tag{8}$$

Assuming the transfer coefficient $\alpha = 0.5$, the effective overpotential increases exponentially with the contact area loss, as shown in Fig. 7b. Severe contact loss (< 50 % of contact) occurs when the overpotential is larger than 0.15 V (50 % increase of the initial value). With the larger overpotential, the predicted steady-state contact area fraction may not be stable or achievable due to possible material degradation. Therefore, the tolerable steady-state contact area fraction for stable cycling should fall within small overpotentials. If we impose a criterion, such that the minimum tolerable contact should be above 80 % (with a 10 % overpotential increase, Fig. 7b), even the Li/Li$_2$O interface requires a stack pressure of about $P_s > 0.05Y_0$. To keep the same contact area fraction, which is larger than 80 %, the less lithiophilic Li/LLZO interface and the lithiophobic Li/LiF interface, require stack pressures of $P_s > 0.5Y_0$ and $P_s > 2Y_0$, respectively.

The model predictions qualitatively and quantitatively agreed with some experimental observations. In recent works (Eckhardt et al., 2023; Zhang et al., 2020; Krauskopf et al., 2019), with both measured and simulated impedance spectra, the contact for the Li/LLZO interface was estimated. It was claimed that a contact area fraction of 96 % is achieved when the stack pressure is increased to about $P_s = 3Y_0$ (since they assumed $Y_0 = 16 \pm 2$MPa, the predicted P_s is around 40 MPa) during stripping (Eckhardt et al., 2023; Zhang et al., 2020). This agreed well with our prediction that a stack pressure between $P_s = 3Y_0 \sim 4Y_0$ can reach almost 100 % steady-state contact area fraction. They also reported a relatively small interface impedance (150 Ωcm^2), which inversely scales with contact area fraction, at about $P_s = 1Y_0 \sim 2Y_0$ and considered the contact area to be around 71 %. This is still reasonable since our interface structures do not include any interphase formed at the Li/LLZO interface. If the interlayer is more lithiophobic in nature (e.g. more Li$_2$CO$_3$), the predicted contact area will shift to a place between the green and blue curves in Fig. 7a. This suggests our model can capture the contact in response to the stack pressure.

Some discrepancies between the model prediction and experimental observations also suggested possible missed mechanisms and future directions. Experimentally Wang et al. (2019), have assigned 'critical stack pressures' for different current densities to prevent large overpotentials. The prediction in Fig. 7a is not very sensitive to the stripping rate within the range of 1 and 10^3 mA/cm^2. This is different from some experimental observations (e.g. Wang et al. (2019)). One reason is that our mapping of the macroscopic creep rate to the hopping rates may overestimate the impact of stack pressure, as forward hopping is always faster than backward hopping rates (according to Eq. (5) and Eq. (6)). As the modified hopping rates ($> 10^7$ s^{-1}) are always larger than the stripping rates (8-8000 s^{-1}), the contact is more sensitive to the stack pressure rather than the stripping current density. Another reason may be the ignorance of possible interface/interphase damage occurring over time and along with the higher current density. This is possible and explains another discrepancy. For example, to interpret the decreasing contact after 32 h of stripping, Wang et al. also decreased their measured strain rates from mechanical tests by 10^{-4} (Wang et al., 2019), similar to Zhang et al. (2020) (shown in Fig. 2c). It is also possible that some damage/change occurs, such as forming inorganic interphase interfaces that are more resistant to creep. For example, less deformable impurities inside the Li metal (e.g. oxide in the grain boundaries) may accumulate at the interface after Li is stripped (Lewis et al., 2021). The Li surface becomes less metallic while forming oxides or other inorganic compounds after interface reaction under higher overpotentials (Shishvan et al., 2023). These interface chemical changes will make the interface more rigid and less deformable. Moreover, the associated interface/interphase damage may also slow down interface hopping or make the interface more lithiophobic at higher current densities. Meanwhile, stack pressures and interface reactions may generate larger local stress near the damaged region, which could accelerate the degradation or cause volume change reflected as "creep" like behavior over a long time. Another possible complexity is the effect of hydrostatic stress. It has been reported that large pressures can induce a significant change in the creep rate (Haslam et al., 2022). However, in this work, we consider a moderate pressure scenario where the hydrostatic stress effect on creep rate is secondary.

5. Conclusions

With the FEM-DFT-KMC simulation, we predicted the multiscale steady-state contact at the Li/SE interface considering interface interactions, stack pressure-induced creep effects, and stripping process. Without stack pressures, the steady-state contact area fraction would be governed by interface interactions following the rank Li/Li_2O (representing extremely lithiophilic interface) >Li/LLZO > Li/LiF (representing extremely lithiophobic interface), while only Li/Li_2O can stabilize a moderate contact ($\sim$ 75 %) for reversible cycling. Moreover, the contact area fraction increases with increasing stack pressure. Using the 80 % of contact as the criteria for stable cycling, when scaled with the Li yield strength (Y_0), the required stack pressures are $P_s > 0.1\ Y_0$, $P_s > 0.5Y_0$, and $P_s > 2Y_0$ at the Li/Li_2O, Li/LLZO, and Li/LiF, respectively. This agreed with experimental observation and the definition of hardness that the full contact can be reached when the stack pressure is $> 3Y_0$. Furthermore, our model showed the steady-state contact area fraction is not sensitive to the stripping current density. Such steady-state contact may not be observed in experiments possibly due to the overestimated creep effects or overpotential-induced material degradation (such as the formation of lithiophobic interlayers), especially under higher current densities (> 10 mA/cm^2). The mechanisms for electrochemical-mechanical coupling in material degradation and interface reactions would help understand the discrepancy with experiments. Thus, comparing predictive multiscale modeling results with experiments, as opposed to using phenomenological models that fitted to experiments, can help to enhance the mechanistic understanding. We believe it is more important to quantify the contact area fraction than to track the void evolution. Based on the predicted steady-state contact area fraction and overpotentials, both appropriate stack pressures and lithiophilic coating materials should be applied to achieve the steady-state contact area fraction for stable cycling of the solid-state batteries using Li metal anodes.

Author Statement

We declare that we did not use any generative AI or AI-assisted technologies in the writing process.

CRediT authorship contribution statement

Min Feng: Writing – review & editing, Writing – original draft, Methodology, Investigation, Formal analysis, Data curation, Conceptualization. **Xing Liu:** Writing – review & editing, Writing – original draft, Methodology, Investigation, Data curation. **Stephen J. Harris:** Writing – review & editing, Conceptualization. **Brian W. Sheldon:** Writing – review & editing, Investigation, Conceptualization. **Yue Qi:** Writing – review & editing, Writing – original draft, Supervision, Software, Resources, Project administration, Methodology, Investigation, Funding acquisition, Formal analysis, Conceptualization.

Declaration of competing interest

The authors declare that they have no known competing financial interests or personal relationships that could have appeared to influence the work reported in this paper.

Data availability

Data will be made available on request.

Acknowledgements

Supplementary materials

Supplementary material associated with this article can be found, in the online version, at doi:10.1016/j.jmps.2024.105878.

References

Abaqus, 2010. Abaqus Reference Manuals (Dassault Systèmes Simulia).
Afferrante, L., Bottiglione, F., Putignano, C., Persson, B.N.J., Carbone, G., 2018. Tribol. Lett. 66, 75.
Agier, J.A.B., Shishvanb, S.S., Flecka, N.A., Deshpandea, V.S., 2022. Acta Mater 240.
Andersen, M., Panosetti, C., Reuter, K., 2019. Front. Chem. 7, 00202.

Barai, P., Fuchs, T., Trevisanello, E., Richter, H.F., Janek, J., Srinivasan, V., 2024. Chem. Mater.

Betz, J., Bieker, G., Meister, P., Placke, T., Winter, M., Schmuch, R., 2019. Adv. Energy Mater. 9, 1803170.

Bortz, A.B., Kalos, M.H., Lebowitz, J.L., 1975. J. Comput. Phys. 17, 10.

Burov, S.A., Boev, O.A., Abakumov, M.A., Aksyonov, A.D., 2024. Phys. Rev. B 109, 045305.

Doux, J.M., Nguyen, H., Tan, D.H.S., Banerjee, A., Wang, X., Wu, E.A., Jo, C., Yang, H., Meng, Y.S., 2020. Adv. Energy Mater. 10, 1903253.

Eckhardt, K.J., Fuchs, T., Burkhardt, S., Klar, J.P., Janek, J., Heiliger, C., 2023. Adv. Mater. Interfaces 10.

Feng, M., Yang, C.-T., Qi, Y., 2022. J. Electrochem. Soc. 169, 090526.

Fincher, D.C., Ojeda, D., Zhang, Y., Pharr, M.G., Pharr, M., 2020. Acta Mater. 186, 215.

Gavilán-Arriazu, M.E., Mercer, P.M., Barraco, E.D., Hoster, E.H., Leiva, M.P.E., 2021. Prog. Energy 3.

Haslam, C., Wolfenstine, J.B., Sakamoto, J., 2022. J. Power Sources 520.

He, X., Ji, X., Zhang, B., Rodrigo, D.N., Hou, S., Gaskell, K., Deng, T., Wan, H., Liu, S., Xu, J., Nan, B., Lucht, L.B., Wang, C., 2022. ACS Energy Lett. 7, 131.

Henkelman, G., Jónsson, H., 2000. J. Chem. Phys. 113, 9978.

Huang, Z., Chen, L., Huang, B., Xu, B., Shao, G., Wang, H., Li, Y., Wang, C.-A., 2020. ACS Appl. Mater. Interfaces 12, 56118.

Janek, J., Zeier, G.W., 2023. Nat. Energy 8, 230.

Jolly, S.D., Ning, Z., Darnbrough, E.J., Kasemchainan, J., Hartley, O.G., Adamson, P., Armstrong, J.E.D., Marrow, J., Bruce, G.P., 2020. ACS Appl. Mater. Interfaces 12, 678.

Joubert, D., 1999. Phys. Rev. B 59, 1758.

Kasemchainan, J., Zekoll, S., Spencer Jolly, D., Ning, Z., Hartley, G.O., Marrow, J., Bruce, P.G., 2019. Nat. Mater. 18, 1105.

Krauskopf, T., Hartmann, H., Zeier, W.G., Janek, J., 2019. ACS Appl. Mater. Interfaces 11, 14463.

LePage, W.S., Chen, Y., Kazyak, E., Chen, K.-H., Sanchez, A.J., Poli, A., Arruda, E.M., Thouless, M.D., Dasgupta, N.P., 2019. J. Electrochem. Soc. 166, A89.

Lewis, J.A., Cortes, F.J.Q., Liu, Y., Miers, J.C., Verma, A., Vishnugopi, B.S., Tippens, J., Prakash, D., Marchese, T.S., Han, S.Y., Lee, C., Shetty, P.P., Lee, H.-W., Shevchenko, P., De Carlo, F., Saldana, C., Mukherjee, P.P., McDowell, M.T., 2021. Nat. Mater. 20, 503.

Lin, D., Liu, Y., Cui, Y., 2017. Nat. Nanotechnol. 12, 194.

Liu, H., Cheng, X.-B., Xu, R., Zhang, X.-Q., Yan, C., Huang, J.-Q., Zhang, Q., 2019. Adv. Energy Mater. 9, 1902254.

Liu, Y., Su, H., Li, M., Xiang, J., Wu, X., Zhong, Y., Wang, X., Xia, X., Gu, C., Tu, J., 2021. J. Mater. Chem. A 9, 13531.

Lu, Y., Zhao, C.-Z., Hu, J.-K., Sun, S., Yuan, H., Fu, Z.-H., Chen, X., Huang, J.-Q., Ouyang, M., Zhang, Q., 2022. Sci. Adv. 8.

Masias, A., Felten, N., Garcia-Mendez, R., Wolfenstine, J., Sakamoto, J., 2019. J. Mater. Sci. 54, 2585.

Mortensen, J.J., Hansen, L.B., Jacobsen, K.W., 2005. Phys. Rev. B 71, 1.

Narayan, S., Anand, L., 2018. Extreme Mech. Lett. 24, 21.

Perdew, J.P., Burke, K., Ernzerhof, M., 1996. Phys. Rev. Lett. 77, 3865.

Persson, B.N.J., 2022. Tribol. Lett. 70, 88.

Roy, U., Fleck, A.N., Deshpande, S.V., 2021. Extreme Mech. Lett. 46.

Ruan, Y., Lu, Y., Huang, X., Su, J., Sun, C., Jin, J., Wen, Z., 2019. J. Mater. Chem. A 7, 14565.

Sharafi, A., Kazyak, E., Davis, A.L., Yu, S., Thompson, T., Siegel, D.J., Dasgupta, N.P., Sakamoto, J., 2017. Chem. Mater. 29, 7961.

Shi, P., Cheng, X.-B., Li, T., Zhang, R., Liu, H., Yan, C., Zhang, X.-Q., Huang, J.-Q., Zhang, Q., 2019. Adv. Mater. 31.

Shishvan, S.S., Fleck, N.A., McMeeking, R.M., Deshpande, V.S., 2020. J. Power Sources 456.

Shishvan, S.S., Fleck, N.A., Deshpande, V.S., 2021. J. Power Sources 488, 229437.

Shishvan, S.S., Fleck, N.A., McMeeking, R.M., Deshpande, V.S., 2023. Electrochim. Acta 467.

Shishvan, S.S., Fleck, N.A., McMeeking, R.M., Deshpande, V.S., 2023. Eur. J. Mech. A: Solids 100.

Tariq, S., Ammigan, K., Hurh, P., Schultz, R., Liu, P., Shang, J., 2003. In: Proceedings of the 2003 Particle Accelerator Conference. Portland, OR, USA, p. 1452.

Tian, H.K., Liu, Z., Ji, Y., Chen, L.Q., Qi, Y., 2019. Chem. Mater. 31, 7351.

Vineyard, G.H., 1957. J. Phys. Chem. Solids 3, 121.

Wang, Y., Cheng, Y.-T., 2017. Scr. Mater. 130, 191.

Wang, M.J., Choudhury, R., Sakamoto, J., 2019. Joule 3, 2165.

Yan, H., Tantratian, K., Ellwood, K., Harrison, E.T., Nichols, M., Cui, X., Chen, L., 2022. Adv. Energy Mater. 12, 2102283.

Yang, C.-T., Qi, Y., 2021. Chem. Mater. 33, 2814.

Yang, M., Liu, Y., Nolan, A.M., Mo, Y., 2021. Adv. Mater. 33, 2008081.

Yu, S., Siegel, J.D., 2017. Chem. Mater. 29, 9639.

Zhang, H., Liao, X., Guan, Y., Xiang, Y., Li, M., Zhang, W., Zhu, X., Ming, H., Lu, L., Qiu, J., Huang, Y., Cao, G., Yang, Y., Mai, L., Zhao, Y., Zhang, H., 2018. Nat. Commun. 9, 3729.

Zhang, X., Wang, Q.J., Harrison, K.L., Roberts, S.A., Harris, S.J., 2020. Cell Rep. Phys. Sci. 1, 100012.

Zhao, Q., Stalin, S., Zhao, C.-Z., Archer, L.A., 2020. Nat. Rev. Mater. 5, 229.

Zhao, Y., Wang, R., Martínez-Pañeda, E., 2022. J. Mech. Phys. Solids 167.

Zheng, C., Zhang, J., Xia, Y., Huang, H., Gan, Y., Liang, C., He, X., Tao, X., Zhang, W., 2021. Small 17, 2101326.